buildings

MDPI

Article

Modelling the Smoke Flow Characteristics of a Comprehensive Pipe Gallery Fire with Rectangular Section

Xu Wang [1,2], Zhilan Yao [1,2,*], Yanru Wang [3], Xianzhen Kong [1,2] and Zhengxiu Lv [1,2]

[1] State Key Laboratory of Mountain Bridge and Tunnel Engineering, Chongqing Jiaotong University, Chongqing 400074, China; xuwang@cqjtu.edu.cn (X.W.); 18853726073@163.com (X.K.); 15684177220@163.com (Z.L.)
[2] School of Civil Engineering, Chongqing Jiaotong University, Chongqing 400041, China
[3] School of Civil Engineering, Taizhou University, Jiaojiang, Taizhou 318000, China; yanrupiaoyang@163.com
* Correspondence: zhilanyao0522@163.com

Abstract: In this study, a numerical model of the cable cabin of a comprehensive pipe gallery was established to study the smoke flow diffusion behaviour of a comprehensive pipe gallery fire under a rectangular cross-section. The effects of fire source power (Q = 0.5, 1.0, 1.5, 2.0, 2.5, 3.0 MW) and fire source location (D = 10, 20, 40, 50, 60, 80, 100 m) on the smoke flow characteristics—such as smoke layer height and thickness, longitudinal airflow velocity, and ceiling temperature distribution—were analysed, and the corresponding prediction model was fitted. The results show the following: (1) The height of the smoke layer decreases with increasing fire power, and the predictive model of the smoke layer thickness obtained from the fitting is proportional to the smoke mass flow rate and inversely proportional to the aspect ratio of the pipe gallery. (2) Longitudinal air velocity prediction models of $D < 50$ m and $D \geq 50$ m are fitted, and the average error between them and the numerical simulation values is 9.611%. (3) The temperature decay gradient of the smoke decreases gradually with increasing distance from the fire source, while there is a significant temperature difference between the two sides of the fire source. The average relative errors of the dimensionless temperature rise models fitted upstream and downstream of the fire source in the form of $\frac{\Delta T}{T_0} = Ae^{B(\frac{D-X}{H})+C}$ exponentials with respect to the numerical simulations were 11.688% and 7.296%, respectively. The results of the study can provide a reference for smoke flow and fire prevention and control in comprehensive pipe galleries.

Keywords: comprehensive pipe gallery; rectangular cross-section; fire source power; fire source location

check for updates

Citation: Wang, X.; Yao, Z.; Wang, Y.; Kong, X.; Lv, Z. Modelling the Smoke Flow Characteristics of a Comprehensive Pipe Gallery Fire with Rectangular Section. *Buildings* **2024**, *14*, 1937. https://doi.org/10.3390/buildings14071937

Academic Editor: Humberto Varum

Received: 23 May 2024
Revised: 15 June 2024
Accepted: 21 June 2024
Published: 25 June 2024

Copyright: © 2024 by the authors. Licensee MDPI, Basel, Switzerland. This article is an open access article distributed under the terms and conditions of the Creative Commons Attribution (CC BY) license (https://creativecommons.org/licenses/by/4.0/).

1. Introduction

As one of the most common disasters in urban comprehensive pipe galleries, fire causes serious economic losses and casualties to the global underground space every year [1,2]. In recent years, the rapid development of comprehensive pipe gallery construction and the internal installation of a large number of industrial and civil cables have led to a significant increase in fire incidents. Once a fire occurs, combustion rapidly spreads toxic exhaust throughout the corridor. Simultaneously, due to the limited space within the pipe gallery, the internal environment becomes complex, directly increasing the difficulty of firefighting and damaging the structure of the pipe gallery [3]. As a result, understanding the distribution of post-disaster smoke flow characteristics in comprehensive pipe galleries has become a critical factor in the post-disaster rescue process [4]. In order to minimise structural damage and loss of human life, it is necessary to study the impact of post-disaster smoke flow characteristics in comprehensive pipe galleries to provide a basis for post-disaster rescue and relief work.

Research on the smoke flow characteristics of fire in integrated tube corridors is usually carried out by means of experimental tests or numerical simulations [5,6]. Liu

et al. [7] conducted a test on a circular tunnel with a length of 20 m, an inner diameter of 1.5 m, and an outer diameter of 1.8 m, and analysed the temperature distribution in a closed public tunnel under fire conditions. It was found that the roof temperature directly above the fire source was the highest, the longitudinal temperature decreased with the distance from the fire source, and the horizontal temperature showed obvious stratification. Zhao et al. [8] investigated the effect of fire source power on longitudinal and transverse temperatures using a scaled-down circular tunnel model. They observed that higher fire source power resulted in higher longitudinal and transverse temperatures and the longitudinal temperature showed an exponential decay relationship with increasing distance from the fire source centre. For example, Niu and Li [9] investigated the diffusion process and temperature change in smoke at different times by means of a rectangular tunnel model, which provided a certain reference for fire emergency rescue. Guo et al. [10] investigated the fire evolution process of a tunnel by means of a small-radius-of-curvature L-type utility tunnel model, which was found to have a large influence on the fire evolution process of the tunnel through the radius of curvature of the tunnel and the critical ventilation rate parameter. Zhong et al. [11] used FDS to numerically simulate the smoke bifurcation flow in a longitudinal ventilation tunnel, and analysed the effects of longitudinal ventilation speed on the smoke flow field, smoke temperature distribution, and smoke layer height, and revealed the generation mechanism of smoke bifurcation flow. An et al. [12] investigated the temperature distribution and CO diffusion law when a fire occurred in an L-type comprehensive pipeline corridor through numerical simulation, and obtained a formula for the maximum temperature rise of the roof of the corridor. Liang et al. [13] conducted numerical simulation of a fire in a T-type underground comprehensive pipeline corridor by using the FDS software, and analysed the effect of the change in fire power on the temperature field of the roof of the corridor, and found that the temperature field of the roof of the T-type intersection was significantly reduced. It was found that the peak temperature of the roof of the T-type intersection increased linearly with the power of the fire source.

The above studies mainly analysed the characteristics and distribution of smoke flow spreading in circular, L-type, and T-type cross-sections, while for a common rectangular cross-section, knowledge of the influence of its post-disaster smoke flow characteristics is still insufficient, and there is a lack of corresponding prediction models.

In this study, a rectangular-cross-section comprehensive pipe gallery model was utilized to investigate the impact of different fire source power levels and positions on parameters such as smoke layer height, longitudinal airflow velocity, and temperature beneath the ceiling. The research determined the smoke spread patterns and developed predictive models for the temperature rise upstream and downstream of the fire source. These findings can serve as a reference for fire risk assessment and safety design in comprehensive pipe galleries.

2. Mathematical Model

2.1. Gas Flow Governing Equations

The FDS software solves compressible fluid problems, for when the fluid density changes. In order to analyse the flow in tubes, the continuity equation, energy conservation equation, momentum conservation equation, ideal gas state equation, and gas component conservation equation are mainly included [14,15]. Their specific expressions are as follows:

(1) Continuity equation:

$$\frac{\partial \rho}{\partial t} + \frac{\partial (\rho u_x)}{\partial x} + \frac{\partial (\rho u_y)}{\partial y} + \frac{\partial (\rho u_z)}{\partial z} = 0 \quad (1)$$

where ρ represents density; and u_x, u_y, u_z denote the velocity components along the x, y, and z axes, respectively.

(2) Energy equation:

$$\frac{\partial(\rho H)}{\partial t} + \frac{\partial(\rho u_x H)}{\partial x} + \frac{\partial(\rho u_y H)}{\partial y} + \frac{\partial(\rho u_z H)}{\partial z} = -pdivU + div(\lambda gradT) + \Phi + S_h \quad (2)$$

where H represents the enthalpy of the gas; $pdivU$ represents the work done by the surface force on the micro element; λ represents thermal conductivity; T represents thermodynamic temperature; Φ represents the energy dissipation function; and S_h represents the internal heat source of the micro element.

(3) Momentum equation:

$$\frac{\partial(\rho u_x)}{\partial t} + \frac{\partial(\rho u_x u_x)}{\partial x} + \frac{\partial(\rho u_x u_y)}{\partial y} + \frac{\partial(\rho u_x u_z)}{\partial z} = -\frac{\partial P}{\partial x} + \mu\left(\frac{\partial^2 u_x}{\partial x^2} + \frac{\partial^2 u_x}{\partial y^2} + \frac{\partial^2 u_x}{\partial z^2}\right) + F_x \quad (3)$$

$$\frac{\partial(\rho u_y)}{\partial t} + \frac{\partial(\rho u_x u_y)}{\partial x} + \frac{\partial(\rho u_y u_y)}{\partial y} + \frac{\partial(\rho u_y u_z)}{\partial z} = -\frac{\partial P}{\partial y} + \mu\left(\frac{\partial^2 u_y}{\partial x^2} + \frac{\partial^2 u_y}{\partial y^2} + \frac{\partial^2 u_y}{\partial z^2}\right) + F_y \quad (4)$$

$$\frac{\partial(\rho u_z)}{\partial t} + \frac{\partial(\rho u_x u_z)}{\partial x} + \frac{\partial(\rho u_y u_z)}{\partial y} + \frac{\partial(\rho u_z u_z)}{\partial z} = -\frac{\partial P}{\partial z} + \mu\left(\frac{\partial^2 u_z}{\partial x^2} + \frac{\partial^2 u_z}{\partial y^2} + \frac{\partial^2 u_z}{\partial z^2}\right) + F_z \quad (5)$$

where μ represents dynamic viscosity, and F_x, F_y, and F_z are the force components in the x, y and z axes, respectively.

(4) Gas state equation:

$$PV = nRT \quad (6)$$

where P represents pressure, V represents volume, n represents the number of moles of gas, R represents the universal gas constant, and T represents the absolute temperature.

(5) Species transport equation:

$$\frac{\partial(\rho w)}{\partial t} + \frac{\partial(\rho u_x w)}{\partial x} + \frac{\partial(\rho u_y w)}{\partial y} + \frac{\partial(\rho u_z w)}{\partial z} = \rho D_t\left[\frac{\partial}{\partial x}\left(\frac{\partial w}{\partial x}\right) + \frac{\partial}{\partial y}\left(\frac{\partial w}{\partial y}\right) + \frac{\partial}{\partial z}\left(\frac{\partial w}{\partial z}\right)\right] \quad (7)$$

where w represents the mass fraction of gas components; and D_t represents the turbulent diffusion coefficient.

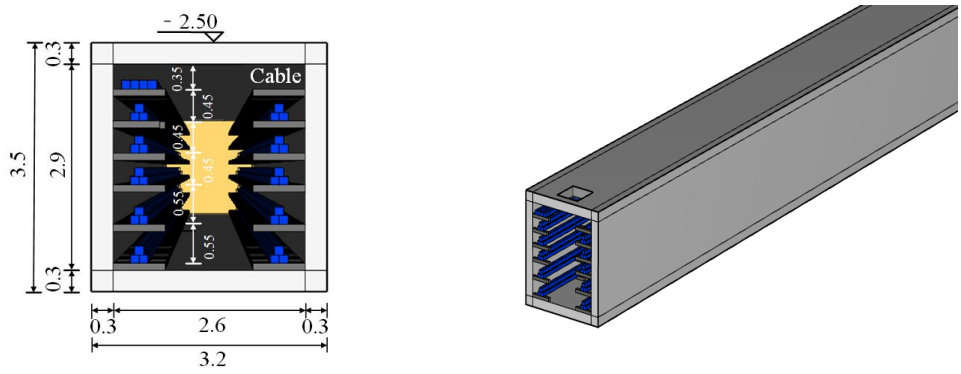
2.2. Combustion Model

A hybrid fractional combustion model was employed, ensuring that the sum of all gas mixture fractions satisfied the conservation law throughout the simulation process.

3. FDS Model

3.1. Model Setup

This study investigates a rectangular cross-section of a comprehensive pipe gallery's cable compartment, employing FDS software to analyse smoke flow characteristics in fire scenarios. Its main structure is made of reinforced concrete with a burial depth of 2.5 m, area dimensions of 3.2 m × 3.5 m × 200 m, and the wall plate of the pipe gallery is made of 0.3 m thick concrete. Additionally, there are a 0.3 m air inlet and outlet sections located 0.9 m × 0.9 m from the closed section of the pipe gallery configuration. The cables are arranged in layers on both sides of the cable rack, as depicted in Figure 1.



(**a**) (**b**)

Figure 1. Rectangular cross-section: (**a**) Cross-section, (**b**) stereo view.

3.1.1. Source of Fire and Type of Reaction

Fire power is considered a crucial factor influencing fire size. In this study, six different fire power levels ranging from 0.5 to 3.0 MW, with intervals of 0.5 MW, are employed. For the most unfavourable scenario, the fire source is positioned below the lowest cable on the left side, covering an area of 0.5 m × 1.0 m. To maintain symmetry within the comprehensive pipeline gallery, the longitudinal position of the fire source is set at 10, 20, 40, 50, 60, 80, and 100 m from the left closed section of the corridor for the study. Due to the complexity of cable reactions during combustion, the main component of the cable material is assumed to be polyvinyl chloride, with a metal conductor. Only the combustion of the cable insulation and sheath material is considered.

3.1.2. Materials and Related Parameters

The relevant parameters of the cable and concrete used in the model are shown in Tables 1 and 2. The cable support is made of steel, which does not burn and is arranged at intervals of 5 m.

Table 1. Cable material characteristic parameters.

Attribute	Numerical Value
Density	1380 kg/m^3
Specific heat	1.289 kJ/kg·K
Electric conductivity	0.192 W/(m·K)

Table 2. Concrete material characteristic parameters.

Attribute	Numerical Value
Density	2280 kg/m^3
Thermal conductivity	1.04 kJ/kg·K
Electric conductivity	1.28 W/(m·K)
Radiation rate	0.9

3.1.3. Gridding and Sensitivity Verification

To facilitate the analysis of smoke volume and temperature changes within the cable compartment, slices are set up on the longitudinal cross-section at the fire source location. Thermocouples, velocity monitoring points, and detectors for gases such as CO, O^2, and CO^2 are installed every 5 m to monitor the changes in smoke volume and temperature. The specific arrangement of these measurement points is shown in Figure 2.

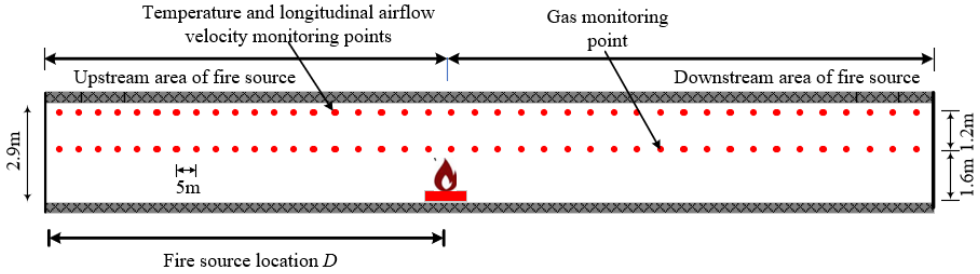


Figure 2. Facade monitoring points.

3.2. Measurement Point Arrangement

To obtain more precise results, this study validates the grid sensitivity by comparing the flame diameter (D^*) with the grid size (δ_x). The calculation formula is as follows:

$$D^* = \left(\frac{Q}{\rho_0 c_p T_0 \sqrt{g}}\right)^{\frac{2}{5}} \tag{8}$$

where Q represents the fire source power; ρ_0 represents the air density; c_p represents the specific heat of air; T_0 represents the ambient air temperature; and g stands for gravitational acceleration.

Taking a fire source power of 3 MW and a fire source position at 10 m as examples, the grid sensitivity is verified using five different grid sizes. The variation in temperature with time at the measurement point directly above the fire source for different grid sizes is shown in Figure 3. From the figure, the temperature below the ceiling increases with the decrease in grid size and tends to stabilize at a constant value. When the grid sizes are 0.1 and 0.05 m, the temperatures at the measurement point are essentially the same, although the computation time is longer for the 0.05 m grid size. Therefore, considering the impact of various fire source powers and computer performance, a grid size of 0.1 m is selected.

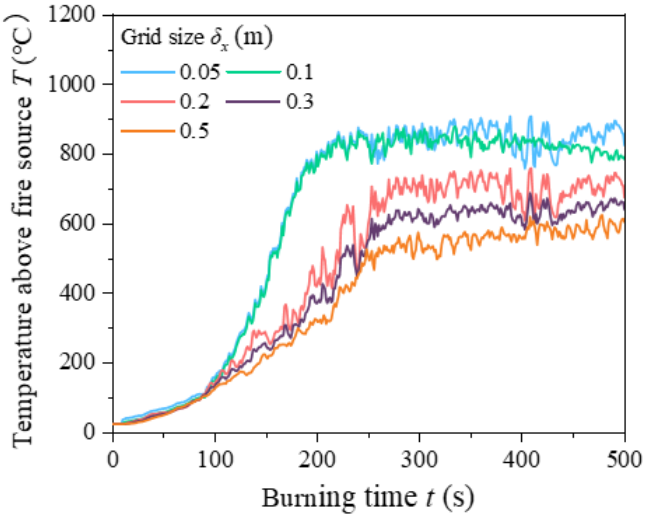


Figure 3. Ceiling temperature changes with time under different grid sizes.

3.3. Model Validation

This study uses the experimental model and results of Han et al. [16] as a reference, employing methane combustion to validate the simulation results for different fire source powers and environmental temperatures, as shown in Figure 4. The figure reveals a trend where temperatures are higher beneath the ceiling directly above the fire source's centre, with lower temperatures on either side. During experiments with fire source powers

of 2.24, 4.21, and 7.69 kW, the highest measured temperatures are 395.06, 446.271, and 504.581 °C, respectively. In comparison, the highest temperatures obtained from FDS simulations were 382.27, 432.781, and 485.766, respectively. This indicates that the highest temperatures measured in the numerical simulations are slightly lower than those recorded in the experiments. Additionally, at positions farther from the fire source, the results from FDS numerical simulations align closely with experimental values. Therefore, the overall simulation results from FDS correspond well with actual experimental outcomes, further validating the effectiveness of the FDS numerical simulations.

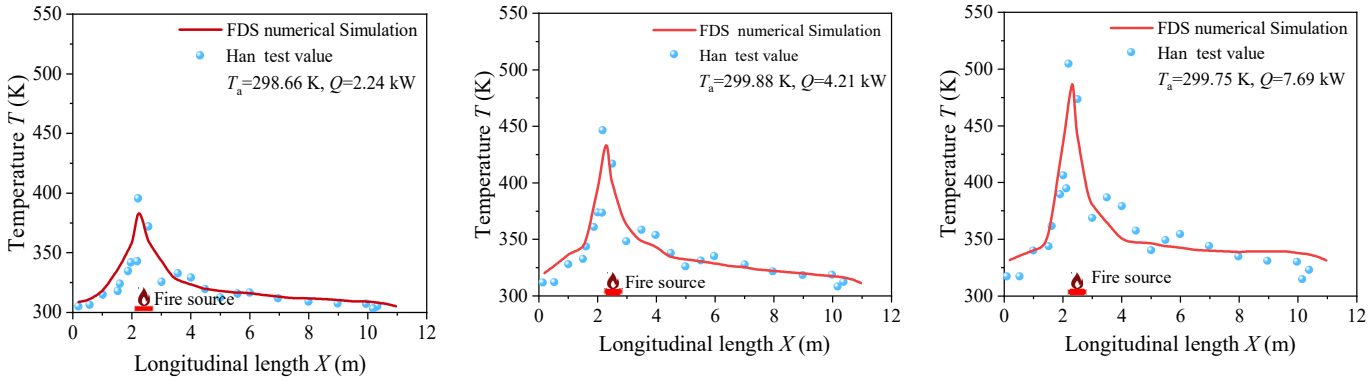


Figure 4. Comparison of methane combustion test and numerical simulation results: (**a**) 2.24 kW; (**b**) 4.21 kW; and (**c**) 7.69 kW.

3.4. Simulation of Working Conditions

In this study, six different fire source powers (0.5, 1.0, 1.5, 2.0, 2.5, 3.0 MW) and seven different fire source positions (10, 20, 40, 50, 60, 80, 100 m) are designed to study the smoke flow characteristics of the combustion stage of the fire in the comprehensive pipe gallery, and to explore the effects of smoke spread and temperature field distribution, the specific working conditions are shown in Table 3.

Table 3. Simulated condition.

Section Shape	Fire Source Power Q (MW)	Fire Source Location D (m)
Rectangular section	0.5 1.0 1.5 2.0 2.5 3.0	10, 20, 40, 50, 60, 80, 100

4. Fire Smoke Flow Characteristics

4.1. Smoke Layer Height and Thickness

The height and thickness of the smoke layer are important parameters that characterize the structural features of the smoke layer in a fire scenario. Figure 5 shows the smoke structure characteristics in the comprehensive pipe gallery fire scenario, primarily divided into four stages: free-rising plume, radial spread, transition, and one-dimensional horizontal spread [17].

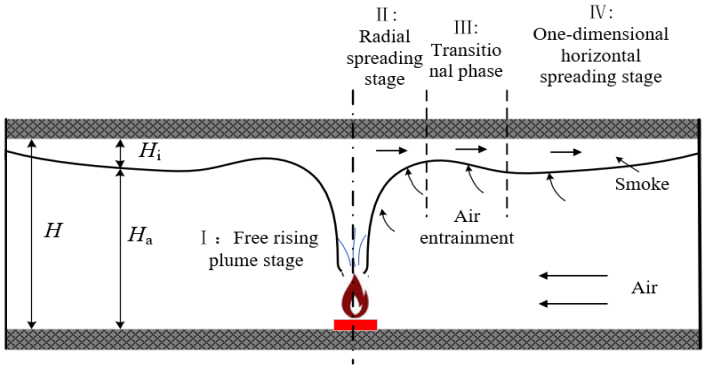


Figure 5. Schematic diagram of smoke structure characteristics.

4.1.1. Smoke Layer Height

The smoke layer height (H_a) is defined as the distance from the bottom of the pipe gallery to the interface of the smoke layer. Taking the centre of the fire source as an example, Figure 6 shows the smoke layer height varies with the longitudinal distance from the fire source under different fire source powers. From the figure, the smoke layer height decreases as the fire source power increases, with heights of 1.34, 1.12, and 0.98 m corresponding to fire source powers of 0.5, 2.0, and 3.0 MW, respectively. Additionally, when the longitudinal distance from the fire source (X_h) is less than 20 m, the smoke layer height increases with increasing distance from the fire source. However, when X_h exceeds 20 m, the smoke layer height no longer changes significantly with distance. At this time, the smoke layer height corresponding to fire source powers of 0.5, 1.0, 1.5, 2.0, 2.5, and 3.0 MW is stable around 1.34, 1.20, 1.15, 1.13, 1.07, and 0.97 m, respectively.

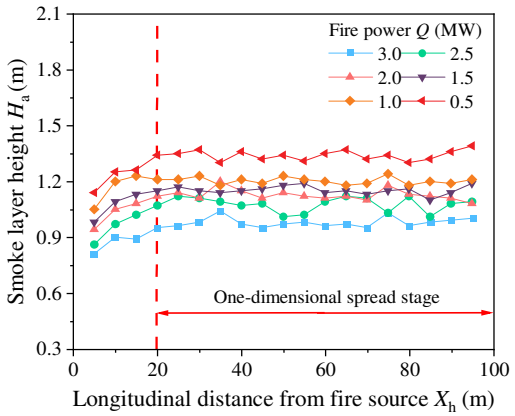


Figure 6. The relationship between the height of the smoke layer and the longitudinal distance from the fire source.

4.1.2. Smoke Layer Thickness

Smoke layer thickness (H_i) is defined as the distance from the ceiling surface of the pipe gallery to the interface of the smoke layer. In this study, based on Fan et al. [18], the pipe gallery aspect ratio (B/H) was used in the calculation of the flue gas layer thickness, and the resulting relationship between the flue gas layer thickness and the variation in the flue gas mass flow rate is shown in Figure 7. From the figure, the smoke layer thickness is directly proportional to the smoke mass flow rate and inversely proportional to the aspect ratio of the pipe gallery and the prediction model of the smoke layer thickness at the one-dimensional horizontal spread stage of the comprehensive pipe gallery is fitted, as shown in Equation (9). Figure 8 compares the smoke layer thickness predictive model of this study with those of other scholars. As shown in the graph, the results of the predictive model in this study are all higher than the results of Xu et al. [19], Gao et al. [20], Tang

et al. [21], and Yang et al. [22]. This could be attributed to the difficulty in evacuating smoke in the enclosed conditions of a comprehensive pipe gallery, leading to an increase in thickness when the smoke layer stabilizes and a decrease in smoke layer height.

$$H_i = 1.18\left(\frac{m_p}{(B/H)^2}\right)^{1/3} + 0.05 \quad (9)$$

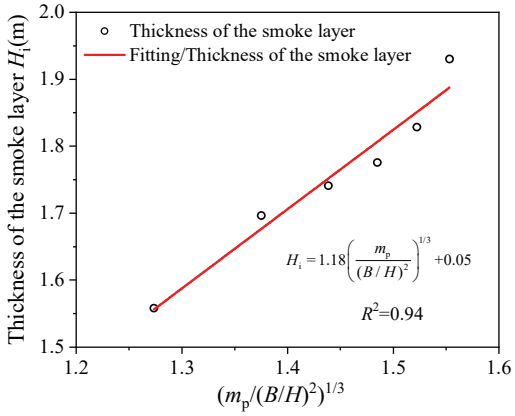


Figure 7. $(m_p/(B/H)^2)^{1/3}$ relationship with the height of the flue gas layer.

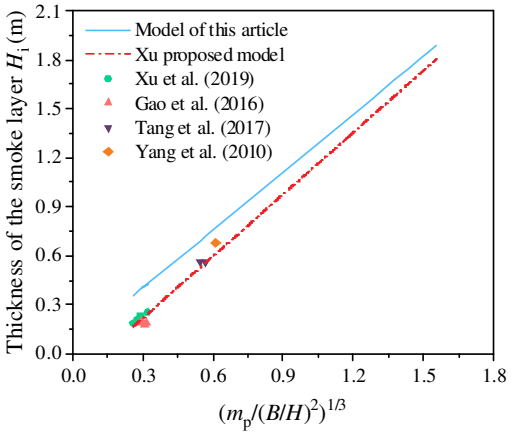
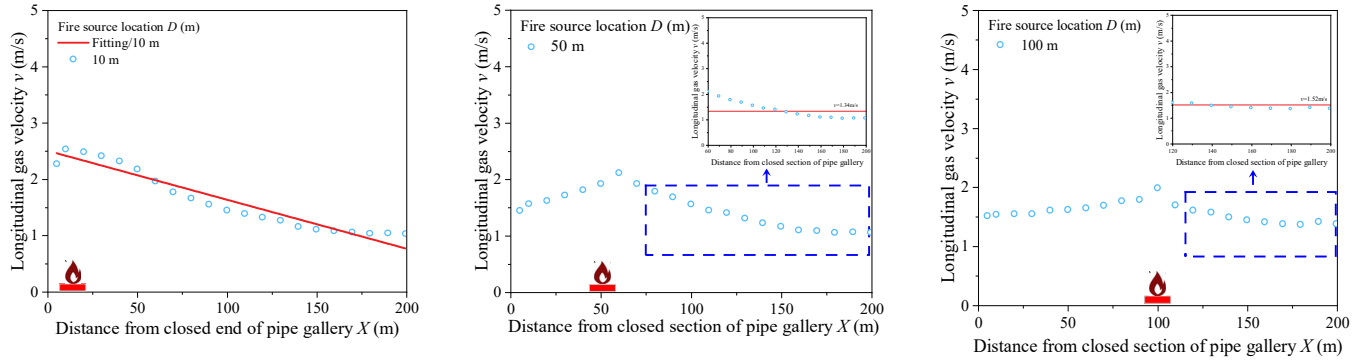


Figure 8. Comparison between the calculated values of the prediction model and the numerical simulation values [19–22].

4.2. Longitudinal Airflow Velocity

The longitudinal airflow velocity within a comprehensive pipe gallery has a significant impact on the temperature distribution during fires and the response time of different monitoring systems. In this study, using a fire source power of 3 MW as an example, the longitudinal airflow velocity is illustrated in Figure 9. From the figure, the longitudinal airflow velocity above the fire source is significantly higher than at other locations, reaching a maximum of 2.54 m/s. This could be attributed to the higher temperature near the fire source, leading to turbulence in the flow field and an increase in airflow velocity. Simultaneously, when the distance of the fire source from the closed section on the left side of the pipe gallery is $D < 50$ m, the longitudinal airflow velocity on the left side of the fire source is higher than that on the right side of the fire source. This could be due to the higher temperature of the smoke on the left side. As the smoke mixes with fresh air it recirculates back towards the enclosed section of the duct, resulting in an increase in airflow velocity.



(**a**) (**b**) (**c**)

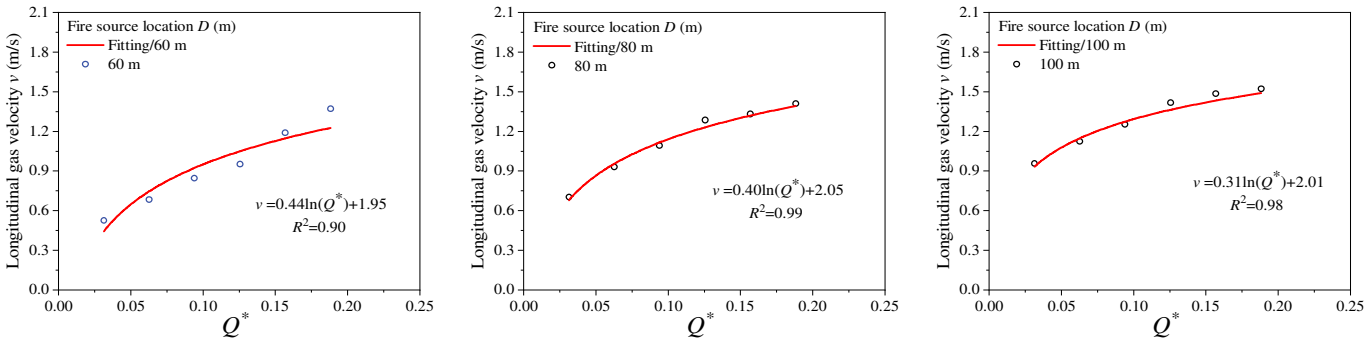
Figure 9. Longitudinal flow velocity when the fire source power is 3 MW: (**a**) D = 10 m, (**b**) D = 50 m, and (**c**) D = 100 m.

In order to further clarify the longitudinal airflow velocity distribution, the dimensionless fire power and fire position were linearly fitted in the form of $v = a_1 x + b_1$ and the specific expressions of the coefficients a_1 and b_1 are shown in Equation (10), and the fitted correlation coefficients are 0.84 and 0.90, respectively.

$$\left.\begin{array}{l} a_1 = 0.0034\frac{D}{L} - 0.013Q^* - 0.0054 \\ b_1 = -0.966\frac{D}{L} + 1.114Q^* + 2.288 \end{array}\right\} \quad (10)$$

When $D \geq 50$ m, in addition to the higher airflow velocity at the centre of the fire source, the airflow velocity at each measurement point differs by no more than 1.0 m/s. Figure 10 shows the variation curve of longitudinal airflow velocity with dimensionless fire source power. From the figure, the vertical airflow velocity within the comprehensive pipe gallery increases with the increase in non-dimensional fire source power, exhibiting a logarithmic relationship between the two. A nonlinear fitting similar to Equation (11) is conducted, yielding different fitting coefficients, a_2 and b_2.

$$v = a_2 InQ^* + b_2 \quad (11)$$



(**a**) (**b**) (**c**)

Figure 10. The relationship between longitudinal airflow velocity and fire source power: (**a**) D = 60 m, (**b**) D = 80 m, and (**c**) D = 100 m.

The variation in the fitting coefficient b_2 with fire source location is minimal, with an average value of 1.99. However, a_2 varies greatly with the location of the fire source. Figure 11 shows the relationship between the fitting coefficient a_2 and the dimensionless

fire source location (D/L). From the figure, a_2 decreases with increasing D/L, as shown in Equation (12) and the fitting coefficient is 0.96.

$$a_2 = -0.58\frac{D}{L} + 0.61 \tag{12}$$

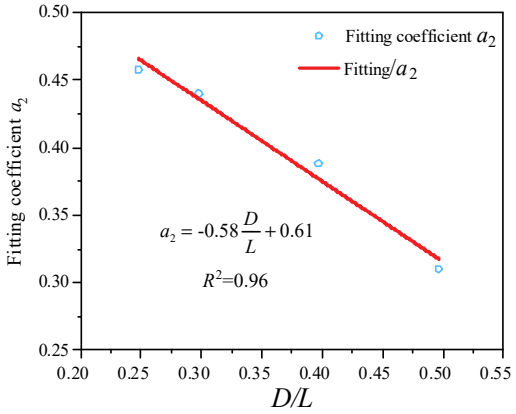


Figure 11. Curve of fitting coefficient a_2 with D/L.

In summary of the above analyses, the longitudinal airflow velocity model for the rectangular-cross-section integrated pipe gallery is established. The specific expression is as follows:

$$v = \begin{Bmatrix} \left(0.0034\frac{D}{L} - 0.013Q^* - 0.0054\right)x - 0.966\frac{D}{L} + 1.14Q^* + 2.288, D < 50m \\ \left(-0.58\frac{D}{L} + 0.61\right)InQ^* + 1.99, D \geq 50m \end{Bmatrix} \tag{13}$$

where v represents the longitudinal airflow velocity; D represents the location of the fire source; L represents the longitudinal length of the pipe gallery; and Q^* represents the dimensionless fire source power.

To further validate the accuracy of the longitudinal airflow velocity prediction model, numerical simulation results are compared with the calculated values from the predictive model, as shown in Figure 12. From the figure, the predicted calculated values and numerical simulation values are in good agreement, and the average relative error is only 9.611%, which can be used for the prediction of longitudinal airflow velocity in the event of fire in the comprehensive pipe gallery.

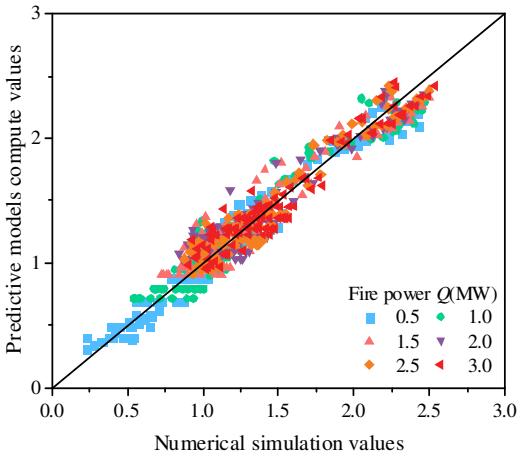


Figure 12. Comparison between the calculated values of the prediction model and the numerical simulation values.

4.3. Longitudinal Temperature Distribution under the Ceiling

The temperature beneath the ceiling of the comprehensive pipe gallery can provide indirect insights into the characteristics of smoke flow. Figure 13 shows the influence of fire source power at various fire source positions on the temperature beneath the ceiling of the comprehensive pipe gallery. From the figure, the ceiling temperature increases with the rise in fire source power. When the fire source is positioned 50 m away from the left enclosed section, the highest temperatures corresponding to fire source powers of 0.5, 1.5, and 3.0 MW are 233, 497, and 736 °C, respectively. When the fire source power remains constant, the temperature beneath the ceiling increases as the fire source position moves closer to the enclosed section of the pipe gallery. Additionally, the gradient of smoke temperature decay decreases gradually with increasing distance from the fire source. For example, when the power of the fire source is 3 MW and the location of the fire source is located in the centre of the pipe gallery, the temperature differences corresponding to the last measuring point of 10, 30 and 50 m from the fire source are 385 °C, 57 °C, and 25 °C, respectively. This phenomenon may be attributed to the fact that at farther distances from the fire source, the increase in ceiling temperature is primarily caused by smoke flow, with less influence from the thermal radiation of the fire source.

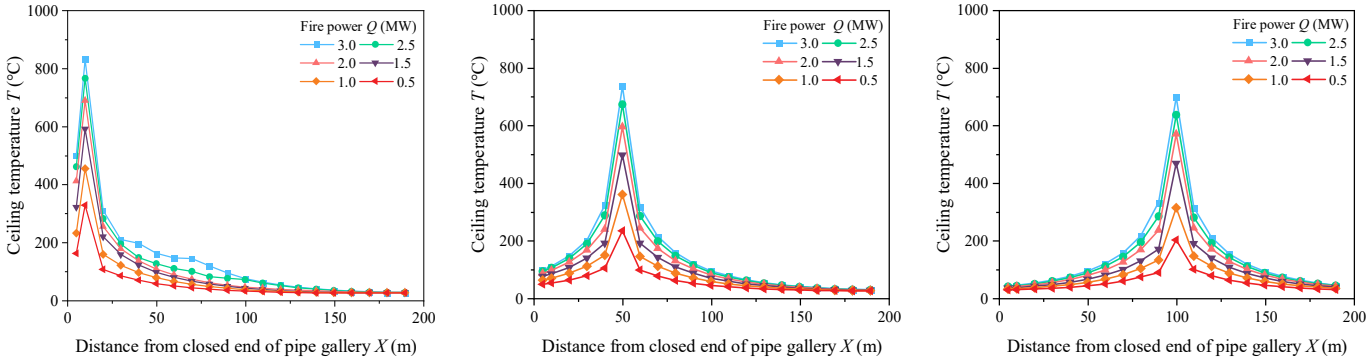


Figure 13. Longitudinal temperature distribution under the ceiling of the integrated pipe gallery: (**a**) D = 10 m, (**b**) D = 50 m, and (**c**) D = 100 m.

Taking a fire source power of 1 MW as an example, Figure 14 shows the temperature distribution at different fire source positions. From the figure, the temperature exhibits a symmetrical distribution along the centre of the fire source. However, when D < 50 m, the temperatures at the left measurement points are significantly higher than those on the right side. For instance, when the fire source position is 20 m, the temperature at the centre of the fire source is 389 °C, while at a point 10 m to the left of the fire source centre, the temperature is 249 °C, and only 145 °C at a point 10 m to the right of the fire source centre. This is mainly due to smoke recirculation caused by the enclosed end leading to a temperature increase. Due to the large temperature difference between the two sides of the fire source, in order to obtain a more accurate predictive model of the dimensionless longitudinal temperature rise of the fire source, it is discussed in terms of the classification of the upstream and downstream sides of the fire source.

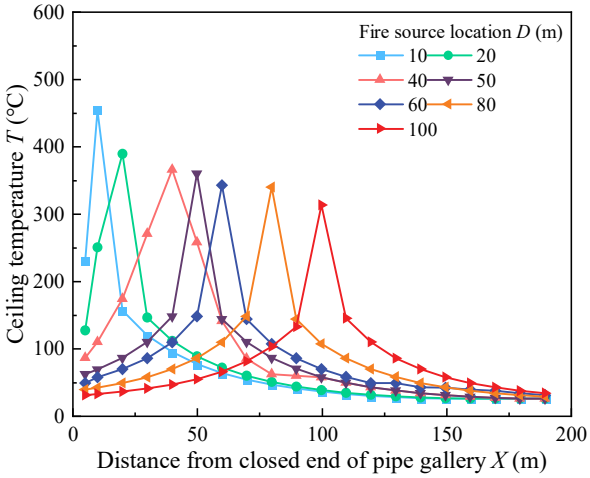


Figure 14. Temperature distribution map of different fire source locations.

4.3.1. Predictive Modelling of Temperature Rise Upstream of the Fire Source

By using the ambient temperature (T_0) and the pipe gallery height (H) as references, the temperature rise ($\Delta T_u/T_0$) at each monitoring point and the distance from the fire source centre ($D - X$) are made dimensionless. Figure 15 shows the relationship between the dimensionless parameter ($\Delta T_u/T_0$) and $(D - X)/H$. As shown in the figure, $\Delta T_u/T_0$ decreases continuously with the increase in $(D - X)/H$, and the rate of decrease gradually diminishes. An exponential fitting similar to Equation (14) is adopted, and the fitting results are presented in Table 4.

$$\frac{\Delta T_{u,d}}{T_0} = A_{u,d} e^{B_{u,d}\left(\frac{D-X}{H}\right)+C_{u,d}} \tag{14}$$

where ΔT_u and ΔT_d represent the longitudinal temperature rise upstream and downstream of the fire source, respectively; X represents the distance of the monitoring point from the left enclosed end of the pipe gallery; A_u, B_u, C_u, and A_d, B_d, C_d are the fitting coefficients for the upstream and downstream of the fire source, respectively.

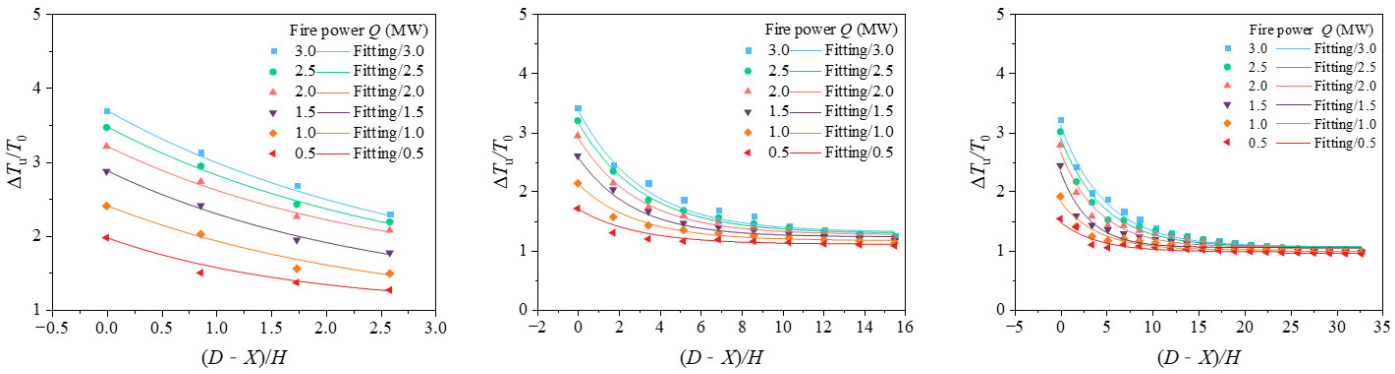


Figure 15. The changing relationship between $(D - X)/H$ and $\Delta T_u/T_0$: (**a**) D = 10 m, (**b**) D = 50 m, and (**c**) D = 100 m.

Table 4. Fitted values of parameters A_u, B_u, and C_u.

		D = 10 m					D = 20 m		
Q	A_u	B_u	C_u	R^2	Q	A_u	B_u	C_u	R^2
0.5	0.944	−0.560	1.031	0.989	0.5	0.695	−0.431	1.190	0.984
1.0	1.469	−0.397	0.943	0.979	1.0	1.097	−0.352	1.179	0.979
1.5	1.748	−0.407	1.136	0.977	1.5	1.447	−0.425	1.193	0.989
2.0	1.805	−0.404	1.414	0.978	2.0	1.961	−0.339	1.193	0.970
2.5	2.177	−0.359	1.305	0.983	2.5	2.203	−0.321	1.183	0.977
3.0	2.401	−0.349	1.301	0.984	3.0	2.407	−0.314	1.172	0.985
Mean value	/	−0.412	1.188	/	Mean value	/	−0.364	1.183	/
		D = 40 m					D = 50 m		
Q	A_u	B_u	C_u	R^2	Q	A_u	B_u	C_u	R^2
0.5	1.115	−0.312	1.208	0.998	0.5	0.601	−0.323	1.098	0.990
1.0	1.518	−0.318	1.191	0.999	1.0	0.964	−0.331	1.161	0.980
1.5	1.677	−0.322	1.190	0.998	1.5	1.361	−0.359	1.223	0.989
2.0	1.818	−0.352	1.186	0.991	2.0	1.649	−0.341	1.262	0.990
2.5	2.020	−0.348	1.185	0.989	2.5	1.892	−0.320	1.282	0.992
3.0	2.222	−0.317	1.199	0.988	3.0	2.080	−0.320	1.304	0.992
Mean value	/	−0.329	1.190	/	Mean value	/	−0.333	1.222	/
		D = 60 m					D = 80 m		
Q	A_u	B_u	C_u	R^2	Q	A_u	B_u	C_u	R^2
0.5	0.601	−0.271	1.210	0.983	0.5	0.566	−0.238	1.198	0.979
1.0	1.302	−0.276	1.209	0.985	1.0		−0.244		0.978
1.5	1.407	−0.297	1.189	0.984	1.5	1.341	−0.284	1.168	0.975
2.0	1.705	−0.264	1.168	0.987	2.0	1.644	−0.248	1.187	0.982
2.5	1.955	−0.256	1.197	0.989	2.5	1.897	−0.239	1.199	0.986
3.0	2.149	−0.250	1.209	0.991	3.0	2.094	−0.235	1.102	0.987
Mean value	/	−0.269	1.197	/	Mean value	/	−0.248	1.163	/

	D = 100 m			
Q	A_u	B_u	C_u	R^2
0.5	0.505	−0.243	1.069	0.936
1.0	0.824	−0.245	1.099	0.939
1.5	1.295	−0.220	1.142	0.936
2.0	1.61	−0.219	1.148	0.969
2.5	1.855	−0.214	1.152	0.981
3.0	2.063	−0.231	1.155	0.987
Mean value	/	−0.227	1.228	/

From Table 4, it can be seen that the value of the fitting parameter C_u does not differ much under different fire source powers and fire source positions, so the average value of 1.20 under various working conditions is taken as the representative value of C_u. For the fitting parameter B_u, the change in fire source position has a great influence on it. Figure 16 shows the relationship between B_u and dimensionless fire source position (D/H). From the figure, B_u increases with the increase in D/H, and different forms of functions are fitted to it, and it is found that the linear fitting result is relatively good and the correlation coefficient is 0.92; the specific expression is as follows:

$$B_u = 0.006\left(\frac{D}{H}\right) - 0.40 \tag{15}$$

Furthermore, under different fire source positions, A_u increases as the fire source power increases. To further investigate their corresponding relationship, the fire source power is subjected to non-dimensionalization. Figure 17 shows the variation curve in

A_u with respect to the non-dimensionalized fire source power under different fire source positions. Its specific relationship expression is as follows:

$$\left\{ \begin{array}{l} A_{u,d} = a_{u,d} Q^{*\beta_{u,d}} \\ Q^* = \dfrac{Q}{\rho_0 c_p T_0 \sqrt{g} H_d^{5/2}} \end{array} \right\} \tag{16}$$

where a_u, β_u and a_d, β_d represent the fire source upstream and downstream fitting parameters, respectively, and the results of their fire source upstream fitting are shown in Table 5.

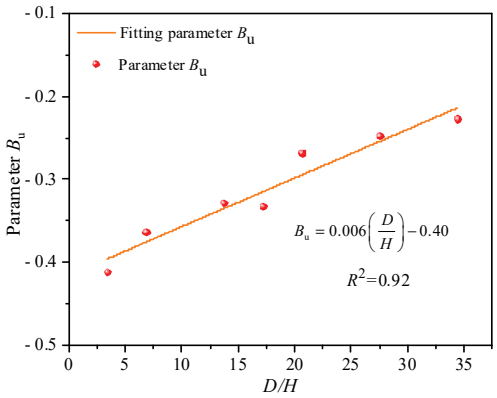


Figure 16. Parameter B_u versus D/H.

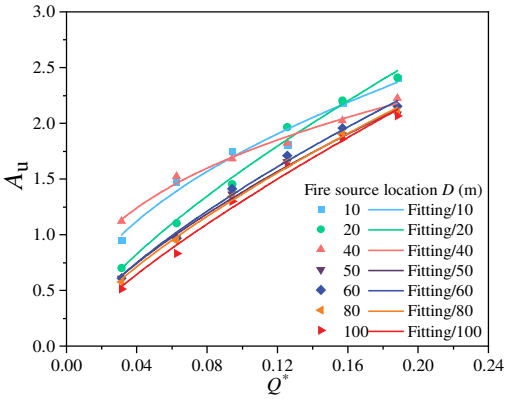


Figure 17. Parameter A_u versus Q^*.

Table 5. Fitted values of parameters α_u and β_u.

D (m)	α_u	β_u
10	5.307	0.785
20	4.782	0.712
40	4.566	0.766
50	4.963	0.684
60	5.974	0.703
80	7.057	0.716
100	7.753	0.778
Mean value	/	0.735

From Table 5, it can be seen that β_u varies less with the position of the fire source and tends to be constant, so its average value of 0.74 is taken. However, α_u varies greatly with the position of the fire source, so the relationship curve of α_u with D/H is drawn, as shown in Figure 18. From the figure, it can be seen that α_u decreases, and then, increases with

the change in D/H, and by fitting it, it is found that the quadratic function has a good agreement. The specific expression is as follows:

$$\alpha_u = 0.005\left(\frac{D}{H}\right)^2 - 0.08\left(\frac{D}{H}\right) + 5.26 \tag{17}$$

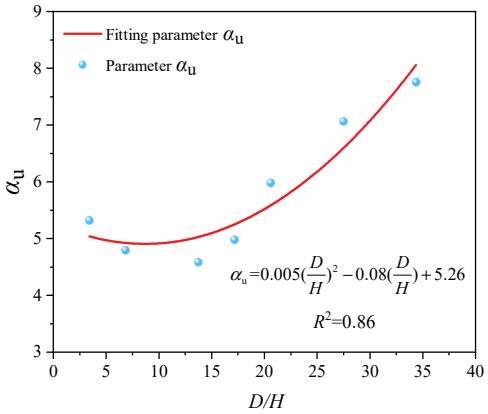


Figure 18. Parameter α_u versus D/H.

Based on Equations (16) and (17), the relationship between A_u and the variations in both fire source power and fire source position can be derived. The specific expression is as follows:

$$A_u = [0.005\left(\frac{D}{H}\right)^2 - 0.08\left(\frac{D}{H}\right) + 5.26]Q^{*0.74} \tag{18}$$

In summary, combining Equations (14), (15), and (18), the dimensionless temperature rise prediction model upstream of the fire source in the comprehensive pipe gallery is obtained:

$$\frac{\Delta T_d}{T_0} = \left[0.005\left(\frac{D}{H}\right)^2 - 0.08\left(\frac{D}{H}\right) + 5.26\right]Q^{*0.74}e^{[0.006(\frac{D}{H})-0.40](\frac{D-X}{H})} + 1.20 \tag{19}$$

In order to verify the reliability of the above model, the value obtained from Equation (19) is compared with the numerical simulation value, as shown in Figure 19. From the figure, the average relative error in the agreement between its predicted and numerically simulated values is 11.688%. Therefore, the model can be used to predict the longitudinal temperature rise in the upstream region of the fire source of the comprehensive pipe gallery.

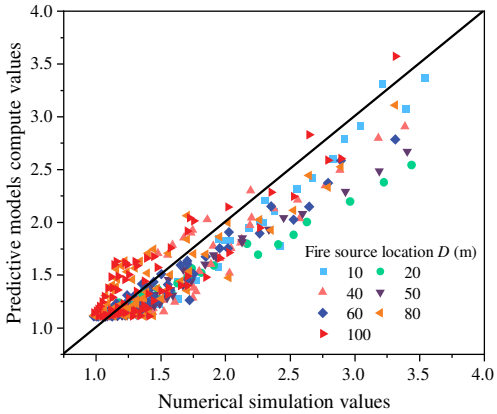


Figure 19. Calculated values of the prediction model and numerical simulation values.

4.3.2. Predictive Modelling of Temperature Rise Downstream of the Fire Source

The temperature rise of each measurement point downstream of the fire source and the distance of the measurement point from the centre of the fire source are processed dimensionlessly, and the relationship curves of $\Delta T_d/T_0$ and $(X-D)/H$ are shown in Figure 20. From the figure, it can be seen that $\Delta T_d/T_0$ decreases with the increase in $(X-D)/H$, and an exponential fit in the form of Equation (14) is carried out, and the fitting results are summarised in Table 6.

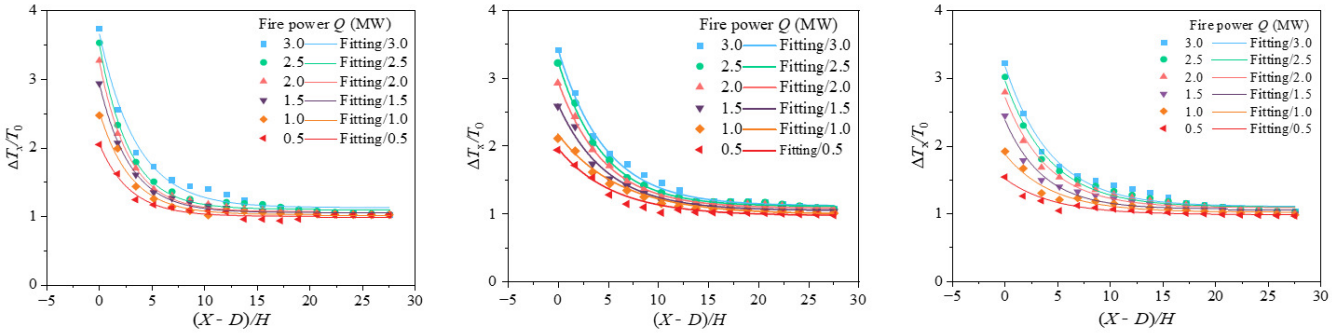


Figure 20. $(X-D)/H$ versus $\Delta T_d/T_0$: (**a**) D = 10 m, (**b**) D = 50 m, and (**c**) D = 100 m.

Table 6. Fitted values of parameters A_d, B_d, and C_d.

D = 10 m					D = 20 m				
Q	A_d	B_d	C_d	R^2	Q	A_d	B_d	C_d	R^2
0.5	1.025	−0.415	1.012	0.996	0.5	0.694	−0.397	1.007	0.925
1.0	1.473	−0.353	1.017	0.992	1.0	1.047	−0.388	1.055	0.918
1.5	1.874	−0.371	1.039	0.996	1.5	1.443	−0.362	1.097	0.931
2.0	2.183	−0.378	1.055	0.996	2.0	1.742	−0.321	1.115	0.951
2.5	2.382	−0.376	1.100	0.990	2.5	1.938	−0.363	1.207	0.966
3.0	2.560	−0.393	1.119	0.982	3.0	2.067	−0.370	1.288	0.944
Mean value	/	−0.386	1.057	/	Mean value	/	−0.367	1.128	/
D = 40 m					D = 50 m				
Q	A_d	B_d	C_d	R^2	Q	A_d	B_d	C_d	R^2
0.5	0.996	−0.281	0.960	0.995	0.5	0.615	−0.299	1.056	0.960
1.0	1.185	−0.264	0.981	0.985	1.0	0.976	−0.291	1.099	0.959
1.5	1.569	−0.308	1.037	0.997	1.5	1.378	−0.302	1.139	0.959
2.0	1.876	−0.318	1.070	0.997	2.0	1.675	−0.268	1.160	0.969
2.5	2.147	−0.326	1.096	0.997	2.5	1.933	−0.244	1.171	0.979
3.0	2.318	−0.312	1.105	0.997	3.0	2.128	−0.243	1.183	0.981
Mean value	/	−0.301	1.041	/	Mean value	/	−0.275	1.135	/
D = 60 m					D = 80 m				
Q	A_d	B_d	C_d	R^2	Q	A_d	B_d	C_d	R^2
0.5	0.612	−0.262	0.993	0.981	0.5	0.555	−0.254	0.983	0.968
1.0	0.977	−0.257	1.034	0.982	1.0	0.919	−0.264	1.025	0.965
1.5	1.428	−0.275	1.072	0.982	1.5	1.323	−0.292	1.067	0.964
2.0	1.733	−0.257	1.097	0.986	2.0	1.630	−0.263	1.086	0.975
2.5	1.978	−0.242	1.114	0.988	2.5	1.880	−0.241	1.098	0.982
3.0	2.176	−0.232	1.125	0.991	3.0	2.092	−0.231	1.107	0.986
Mean value	/	−0.254	1.073	/	Mean value	/	−0.258	1.061	/

D = 100 m				
Q	A_d	B_d	C_d	R^2
0.5	0.530	−0.254	0.976	0.979
1.0	0.854	−0.242	1.012	0.977
1.5	1.309	−0.271	1.058	0.971
2.0	1.630	−0.265	1.076	0.980
2.5	1.862	−0.284	1.088	0.986
3.0	2.068	−0.255	1.095	0.988
Mean value	/	−0.265	1.051	/

From Table 6, it can be seen that the difference in the fitted parameter C_d is small at different fire source powers and fire source locations, so the average value of 1.08 is taken, while B_d increases with the increase in the distance of the fire source from the closed end of the pipe gallery. Figure 21 shows the change relationship between B_d and the position of the dimensionless fire source (D/H), and linear fitting is performed to obtain Equation (20), whose fitting correlation coefficient is 0.87. Compared with the fitting parameters B_u and C_u in the upstream area of the fire source, the slope and intercept have little difference.

$$B_d = 0.005\left(\frac{D}{H}\right) - 0.37 \tag{20}$$

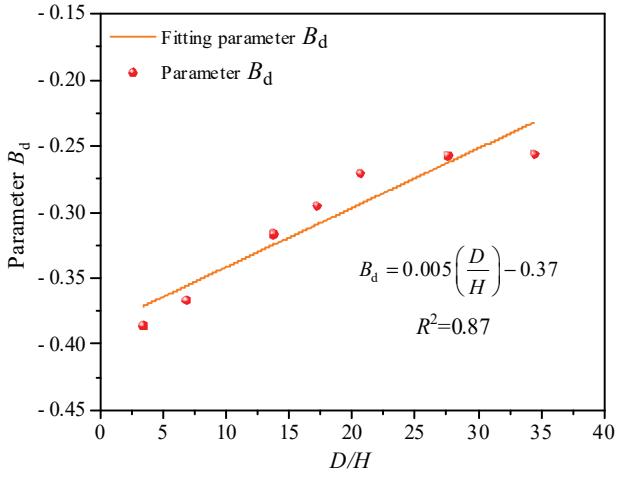


Figure 21. Parameter β_d versus D/H.

In addition, at different fire source locations, A_d increases with increasing fire source power and decreases with increasing distance of the fire source location from the closed end of the pipe gallery. The power relationship curve between A_d and the dimensionless fire source is shown in Figure 22, and nonlinear fitting is carried out as shown in Equation (16). The downstream fitting parameter results of the fire source are shown in Table 6.

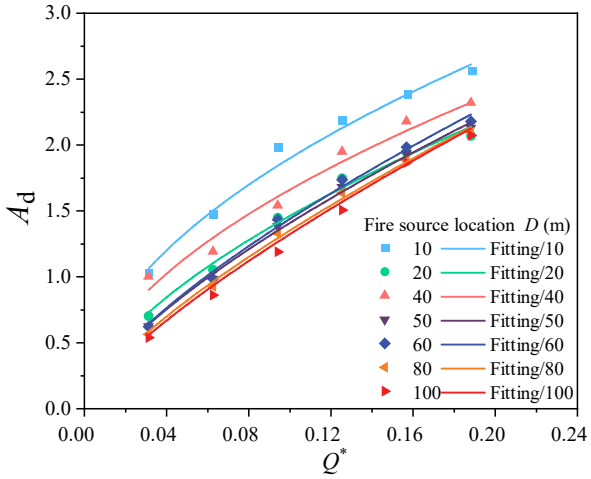


Figure 22. Parameter A_d versus Q^*.

From Table 7, the distance of the fire source centre from the closed end of the pipe gallery (D) has a small effect on the fitting parameter β_d, so its average value of 0.70 is taken, while αd increases with the increase in D. Figure 23 shows the relationship curve between the fitting coefficient α_d and D/H, and the relationship expression between α_d and

D/H is obtained by linear fitting, as shown in (20), which is different and higher than α_u compared to the fitting parameter upstream of the fire source.

Table 7. Fitted values of parameters α_d and β_d.

D (m)	α_d	β_d
10	5.307	0.785
20	4.782	0.712
40	4.566	0.766
50	4.963	0.684
60	5.974	0.703
80	7.057	0.716
100	7.753	0.778
Mean value	/	0.735

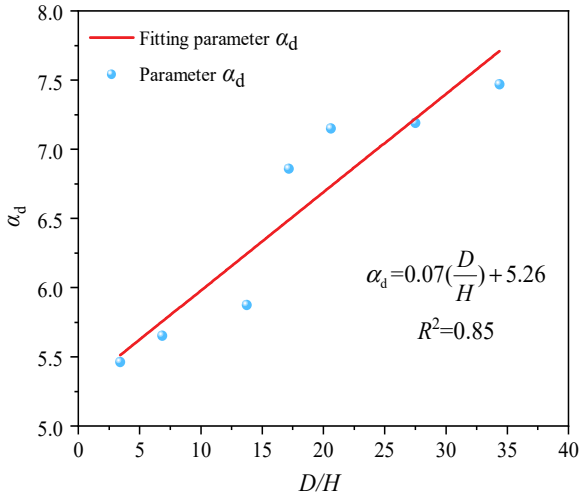


Figure 23. Parameter α_d versus D/H.

$$\alpha_d = 0.07\left(\frac{D}{H}\right) + 5.26 \tag{21}$$

According to Equations (16) and (21), expressions for the relationship of the fitting parameter A_d with the power of the fire source and the distance of the centre of the fire source from the closed end of the pipe gallery are obtained:

$$A_d = \left[0.07\left(\frac{D}{H}\right) + 5.26\right] Q^{*0.70} \tag{22}$$

Combining Equations (14), (20), and (22), the final dimensionless temperature rise prediction model downstream of the fire source is obtained:

$$\frac{\Delta T_d}{T_0} = \left[0.07\left(\frac{D}{H}\right) + 5.26\right] Q^{*0.70} e^{[0.005(\frac{D}{H})-0.37](\frac{X-D}{H})} + 1.08 \tag{23}$$

In order to verify the credibility of the above model, the numerical simulation values were compared with the calculated values of Equation (23), as shown in Figure 24; the average relative error between its predicted and numerically simulated values is 7.296%. Therefore, this model can be used to predict the longitudinal temperature rise in the region downstream of the fire source in the comprehensive pipe gallery.

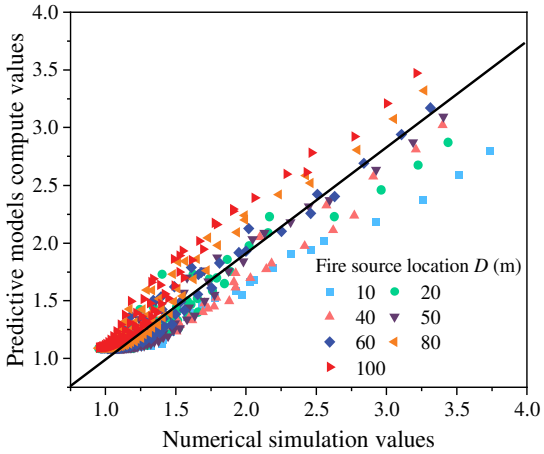


Figure 24. Calculated values of the prediction model and numerical simulation values.

5. Conclusions

In this study, a numerical model of the cable compartment of a rectangular-cross-section comprehensive pipe gallery was established using FDS. Subsequently, the fire smoke flow characteristics of the comprehensive pipe gallery under various fire scenarios were analysed. The study focused on investigating the effects of fire source power and fire source location on the height and thickness of the smoke layer, the longitudinal airflow velocity, and the temperature distribution of the roof during the combustion stage. Based on these analyses, a corresponding prediction model was proposed. The following important conclusions are drawn:

(1) The height of the smoke layer decreases with the increase in fire source power. When the longitudinal distance of the fire source exceeds 20 m, the smoke layer heights corresponding to fire powers of 0.5, 1.0, 1.5, 2.0, 2.5, and 3.0 MW stabilize at 1.34, 1.20, 1.15, 1.13, 1.07, and 0.97, respectively. Additionally, the fitted smoke layer thickness prediction model shows that the smoke layer thickness is directly proportional to the smoke mass flow rate and inversely proportional to the aspect ratio of the pipe gallery.

(2) When the distance between the fire source centre and the closed end of the pipe gallery is less than 50 m, the longitudinal airflow velocity near the closed end significantly exceeds that at the far end. Conversely, when it is greater than or equal to 50 m, the longitudinal airflow velocity is symmetrically distributed around the centre of the fire source, and except for the centre of the fire source, the airflow velocity at each measurement point differs by no more than 1.0 m/s. Additionally, the longitudinal air velocity prediction models of $D < 50$ m and $D \geq 50$ m are fitted and the average error between them and the numerical simulation values is 9.611%.

(3) The temperature decay gradient of the smoke decreases gradually with increasing distance from the fire source, while there is a significant temperature difference between the two sides of the fire source. The average relative errors of the dimensionless temperature rise models fitted upstream and downstream of the fire source in the form of $\frac{\Delta T}{T_0} = Ae^{B(\frac{D-X}{H})+C}$ exponentials with respect to the numerical simulations were 11.688% and 7.296%, respectively.

Author Contributions: Conceptualization and methodology, X.W.; writing—original draft preparation and writing—review and editing, Z.Y.; validation and investigation, Y.W.; visualization and supervision, X.K.; project administration, Z.L. All authors have read and agreed to the published version of the manuscript.

Funding: This paper was partially supported by the Natural Science Foundation of Chongqing (Grant No.: CSTB2022NSCQ-MSX1655) and the State Key Laboratory of Structural Dynamics of Bridge Engineering and Key Laboratory of Bridge Structure Seismic Technology for Transportation Industry Open Fund (Grant No.: 202205).

Institutional Review Board Statement: Not applicable.

Informed Consent Statement: Not applicable.

Data Availability Statement: All data generated or analysed during this study are included in this article. All data included in this study are available upon request by contact with the corresponding author.

Conflicts of Interest: The authors declare no conflicts of interest.

References

1. Yao, Y.; Cheng, X.; Zhang, S.; Zhu, K.; Zhang, H.; Shi, L. Maximum smoke temperature beneath the ceiling in an enclosed channel with different fire locations. *Appl. Therm. Eng.* **2017**, *111*, 30–38. [CrossRef]
2. Liu, F.; Yu, L.X.; Weng, M.C.; Lu, X.L. Study on longitudinal temperature distribution of fire-induced ceiling flow in tunnels with different sectional coefficients. *Tunn. Undergr. Space Technol.* **2016**, *54*, 49–60. [CrossRef]
3. Zhao, Y.C.; Zhu, G.Q.; Gao, Y.J.; Tao, H.J. Study on temperature field of fire smoke in utility tunnel with different cross sections. *Procedia Eng.* **2018**, *211*, 1043–1051. [CrossRef]
4. Wang, F.; Wang, M.; Carvel, R.; Wang, Y. Numerical study on fire smoke movement and control in curved road tunnels. *Tunn. Undergr. Space Technol.* **2017**, *67*, 1–7. [CrossRef]
5. Ji, J.; Bi, Y.; Venkatasubbaiah, K.; Li, K. Influence of aspect ratio of tunnel on smoke temperature distribution under ceiling in near field of fire source. *Appl. Therm. Eng.* **2016**, *106*, 1094–1102. [CrossRef]
6. Fan, C.G.; Li, Y.Z.; Ingason, H.; Lönnermark, A. Effect of tunnel cross section on gas temperatures and heat fluxes in case of large heat release rate. *Appl. Therm. Eng.* **2016**, *93*, 405–415. [CrossRef]
7. Liu, H.N.; Zhu, G.Q.; Pan, R.L.; Yu, M.M.; Liang, Z.H. Experimental investigation of fire temperature distribution and ceiling temperature prediction in closed utility tunnel. *Case Stud. Therm. Eng.* **2019**, *14*, 100493. [CrossRef]
8. Zhao, Y.C.; Zhu, G.Q.; Gao, Y.J. Experimental study on smoke temperature distribution under different power conditions in utility tunnel. *Case Stud. Therm. Eng.* **2018**, *12*, 69–76. [CrossRef]
9. Niu, Y.; Li, W. Simulation study on value of cable fire in the cable tunnel. *Procedia Eng.* **2012**, *43*, 569–573. [CrossRef]
10. Guo, J.; Cai, G.; Liu, Y.; Wen, H.; Jin, Y. Temperature distribution and characteristics induced by fire smoke in L-shaped utility tunnels with small curvature radii. *Case Stud. Therm. Eng.* **2021**, *28*, 101470. [CrossRef]
11. Zhong, W.; Lv, J.; Li, Z.; Liang, T. A study of bifurcation flow of fire smoke in tunnel with longitudinal ventilation. *Int. J. Heat Mass Transfer.* **2013**, *67*, 829–835. [CrossRef]
12. An, W.; Tang, Y.; Liang, K.; Cai, M.; Wang, T.; Wang, Z. Study on temperature distribution and CO diffusion induced by cable fire in L-shaped utility tunnel. *Sustain. Cities Soc.* **2020**, *62*, 102407. [CrossRef]
13. Liang, K.; Hao, X.; An, W.; Tang, Y.; Cong, Y. Study on cable fire spread and smoke temperature distribution in T-shaped utility tunnel. *Case Stud. Therm. Eng.* **2019**, *14*, 100433. [CrossRef]
14. Zhang, P.; Lan, H. Effects of ventilation on leakage and diffusion law of gas pipeline in utility tunnel. *Tunn. Undergr. Space Technol.* **2020**, *105*, 103557. [CrossRef]
15. Tian, Y.; Qin, C.; Yang, Z.; Hao, D. Numerical simulation study on the leakage and diffusion characteristics of high-pressure hydrogen gas in different spatial scenes. *Int. J. Hydrogen Energy.* **2024**, *50*, 1335–1349. [CrossRef]
16. Han, J.; Liu, F.; Wang, F.; Weng, M.; Wang, J. Study on the smoke movement and downstream temperature distribution in a sloping tunnel with one closed portal. *Int. J. Therm. Sci.* **2020**, *149*, 106165. [CrossRef]
17. Jiang, X.; Liu, M.; Wang, J.; Li, K. Study on air entrainment coefficient of one-dimensional horizontal movement stage of tunnel fire smoke in top central exhaust. *Tunn. Undergr. Space Technol.* **2016**, *60*, 1–9. [CrossRef]
18. Fan, W.C.; Wang, Q.G.; Jiang, F.H.; Zhou, J. *An Introduction to Fire Safety Science*; Press of University of Science and Technology of China: Hefei, China, 1995; p. 125. (In Chinese)
19. Xu, Z.; Zhao, J.; Liu, Q.; Chen, H.; Liu, Y.; Geng, Z.; He, L. Experimental investigation on smoke spread characteristics and smoke layer height in tunnels. *Fire Mater.* **2019**, *43*, 303–309. [CrossRef]
20. Gao, Z.H.; Ji, J.; Fan, C.G.; Li, L.J.; Sun, J.H. Determination of smoke layer interface height of medium scale tunnel fire scenarios. *Tunn. Undergr. Space Technol.* **2016**, *56*, 118–124. [CrossRef]
21. Tang, F.; Li, L.J.; Dong, M.S.; Wang, Q.; Mei, F.Z.; Hu, L.H. Characterization of buoyant flow stratification behaviors by Richardson (Froude) number in a tunnel fire with complex combination of longitudinal ventilation and ceiling extraction. *Appl. Therm. Eng.* **2017**, *110*, 1021–1028. [CrossRef]
22. Yang, D.; Hu, L.H.; Huo, R.; Jiang, Y.Q.; Liu, S.; Tang, F. Experimental study on buoyant flow stratification induced by a fire in a horizontal channel. *Appl. Therm. Eng.* **2010**, *30*, 872–878. [CrossRef]

Disclaimer/Publisher's Note: The statements, opinions and data contained in all publications are solely those of the individual author(s) and contributor(s) and not of MDPI and/or the editor(s). MDPI and/or the editor(s) disclaim responsibility for any injury to people or property resulting from any ideas, methods, instructions or products referred to in the content.